AGU PUBLICATIONS

JGR

Journal of Geophysical Research: Space Physics

RESEARCH ARTICLE
10.1002/2014JA020689

Key Points:
- Subionospheric VLF used to detect energetic electron precipitation
- Magnitudes agree with satellite observations but with higher sensitivity
- Variation agrees well with that of lower band chorus

Correspondence to:
C. J. Rodger,
crodger@physics.otago.ac.nz

Citation:
Neal, J. J., C. J. Rodger, M. A. Clilverd, N. R. Thomson, T. Raita, and T. Ulich (2015), Long-term determination of energetic electron precipitation into the atmosphere from AARDDVARK subionospheric VLF observations, *J. Geophys. Res. Space Physics*, *120*, 2194–2211, doi:10.1002/2014JA020689.

Received 6 OCT 2014
Accepted 7 FEB 2015
Accepted article online 11 FEB 2015
Published online 12 MAR 2015

Long-term determination of energetic electron precipitation into the atmosphere from AARDDVARK subionospheric VLF observations

Jason J. Neal[1], Craig J. Rodger[1], Mark A. Clilverd[2], Neil R. Thomson[1], Tero Raita[3], and Thomas Ulich[3]

[1]Department of Physics, University of Otago, Dunedin, New Zealand, [2]British Antarctic Survey (NERC), Cambridge, UK, [3]Sodankylä Geophysical Observatory, University of Oulu, Sodankylä, Finland

Abstract We analyze observations of subionospherically propagating very low frequency (VLF) radio waves to determine outer radiation belt energetic electron precipitation (EEP) flux magnitudes. The radio wave receiver in Sodankylä, Finland (Sodankylä Geophysical Observatory) observes signals from the transmitter with call sign NAA (Cutler, Maine). The receiver is part of the Antarctic-Arctic Radiation-belt Dynamic Deposition VLF Atmospheric Research Konsortia (AARDDVARK). We use a near-continuous data set spanning November 2004 until December 2013 to determine the long time period EEP variations. We determine quiet day curves over the entire period and use these to identify propagation disturbances caused by EEP. Long Wave Propagation Code radio wave propagation modeling is used to estimate the precipitating electron flux magnitudes from the observed amplitude disturbances, allowing for solar cycle changes in the ambient *D* region and dynamic variations in the EEP energy spectra. Our method performs well during the summer months when the daylit ionosphere is most stable but fails during the winter. From the summer observations, we have obtained 693 days worth of hourly EEP flux magnitudes over the 2004–2013 period. These AARDDVARK-based fluxes agree well with independent satellite precipitation measurements during high-intensity events. However, our method of EEP detection is 10–50 times more sensitive to low flux levels than the satellite measurements. Our EEP variations also show good agreement with the variation in lower band chorus wave powers, providing some confidence that chorus is the primary driver for the outer belt precipitation we are monitoring.

1. Introduction

More than 55 years since the discovery of the radiation belts, there are still significant uncertainties about the source, loss, and transport of energetic particles inside the belts [*Reeves et al.*, 2009]. A particle may resonate with different magnetospheric waves, causing simultaneous change in one or more of the particle pitch angle, momentum, or position, which cause the outer radiation belt to be highly dynamic [*Thorne*, 2010], with fluxes of energetic electrons changing by >3 orders of magnitude over time scales of hours to days [*Li and Temerin*, 2001; *Morley et al.*, 2010]. For about the last 10 years, there has been a strong focus by the scientific community on the highly dynamic nature of the radiation belts. This has likely been partially stimulated by the development and launch on 30 August 2012 of NASA's Van Allan Probes, which have the primary scientific goal of understanding the acceleration, transport, and loss processes affecting radiation belt particles.

It has long been recognized that the magnitude of the flux of trapped electrons in the outer radiation belt is a "delicate balance between acceleration and loss" [*Reeves et al.*, 2003], where significant increases or decreases in the trapped electron flux can occur depending on whether the acceleration or loss processes dominate. Energetic electron precipitation (EEP) is one significant loss mechanism for the outer radiation belt [e.g., *Thorne et al.*, 2005; *Morley et al.*, 2010; *Hendry et al.*, 2012; *Ni et al.*, 2013], by which high-energy electrons are lost out of the radiation belts through collisions with the atmosphere. Quantifying the magnitudes of precipitating electron flux as well as their spatial and temporal distributions are important for a full understanding of the radiation belt dynamics, as they also act as an indicator for the mechanisms occurring inside the belts [*Ni et al.*, 2013]. For example, observations have shown that there are consistently very strong dropouts in the outer belt electron fluxes during the small moderate geomagnetic disturbances associated

with the arrival of a high-speed associated solar wind stream interface at the magnetosphere [*Morley et al*., 2010]. Increasing evidence points to the main driver of these dropouts, being magnetopause shadowing [*Turner et al*., 2012] without a significant contribution from electron precipitation during the dropout [*Meredith et al*., 2011]. However, immediately following the dropout, as the acceleration processes start to rebuild the trapped fluxes, there are very significant precipitation levels [*Hendry et al*., 2012] likely due to wave-particle interactions with chorus [*Li et al*., 2013].

There is growing evidence that energetic electron precipitation (EEP) from the radiation belts may play an important role in the chemical makeup of the polar mesosphere, potentially influencing atmospheric dynamics and polar surface climate. It has long been recognized in the radiation belt community that relativistic electron precipitation can provide an additional source of ozone-destroying odd nitrogen [*Thorne*, 1977], leading the author to conclude that the effects of EEP "must also be considered in future photochemical modeling of the terrestrial ozone layer." There is growing evidence in support of this basic idea, albeit concerning mesospheric ozone rather than affects in the stratospheric ozone layer.

Particle precipitation can lead to catalytic ozone destruction due to the reactions with precipitation-produced odd nitrogen and odd hydrogen in the Earth's atmosphere [*Brasseur and Solomon*, 2005]. The first confirmation of this came from experimental observations during solar proton events, where significant ozone destruction occurred in the mesospheric polar atmosphere [e.g., *Seppälä et al*., 2006, 2007]. In addition, there is growing evidence of high levels of energetic electron precipitation (EEP) during both geomagnetic storms and substorms [e.g., *Rodger et al*., 2007a; *Clilverd et al*., 2012]. The EEP intensities in these examples are sufficient to produce significant polar region mesospheric chemical changes [*Rodger et al*., 2010b] of similar magnitude to a medium-sized solar proton event. Mesospheric observation of the EEP chemical changes have now been reported caused by the direct effect of the precipitation (e.g., odd nitrogen [*Newnham et al*., 2011] and odd hydrogen [*Verronen et al*., 2011; *Andersson et al*., 2012, 2014a] with subsequent ozone decreases [*Daae et al*., 2012; *Andersson et al*., 2014b]). Detectable EEP-produced odd hydrogen increases have been reported due to electrons from ~100 keV to ~3 MeV, leading to increases from ~82 km to 52 km altitude [*Andersson et al*., 2012]. Superposed epoch analysis of mesospheric ozone decreases at 70–80 km immediately after EEP events from 2004 to 2009 indicated that the magnitudes of these short-term depletions are comparable to those caused by larger but much less frequent solar proton events [*Andersson et al*., 2014b].

There is evidence that EEP may influence polar surface climate. Large (±2 K) variations in polar surface air temperatures have been produced in chemistry-climate models after NO_x sources were imposed to represent the atmospheric impact of EEP [*Rozanov et al*., 2005; *Baumgaertner et al*., 2011]. These modeling studies have been tested using experimentally derived operational surface level air temperature data sets (ERA-40 and European Centre for Medium-Range Weather Forecasts), examining how polar temperatures vary with geomagnetic activity [*Seppälä et al*., 2009]. This test produced similar patterns in surface level air temperature variability as the modeling studies but with temperatures differing by as much as ±4.5 K between high and low geomagnetic storm periods. It was also found that changing solar irradiance/EUV levels did not drive the observed surface level air temperature variability. *Seppälä et al*. [2009] argued that the primary reason for the temperature variability was most likely EEP causing ozone decreases through NO_x production. More recently, ERA-40 reanalysis data have been examined to see how the EEP-produced atmospheric changes might couple to stratospheric dynamics [*Seppälä et al*., 2013], concluding that that EEP-generated NO_x altered planetary wave breaking in the lower stratosphere. The change in the locations of planetary wave breaking allows more planetary waves to propagate into the upper stratosphere in low latitudes, leading to the observed dynamical responses.

Further studies making use of chemistry-climate models require realistic EEP observations. This has led to increased focus on EEP measurements, as well efforts to incorporate such particle inputs into climate models through the development of systems such as the Atmospheric Ionization Module OSnabrück (AIMOS) model [*Wissing and Kallenrode*, 2009]. AIMOS combines experimental observations from low Earth orbiting and geostationary orbiting spacecraft with geomagnetic observations to provide a 3-D numerical model of atmospheric ionization due to precipitating particles.

One of the most commonly used sources of EEP measurements is the Medium Energy Proton and Electron Detector (MEPED) instrument in the Space Environment Monitor-2 (SEM-2) experimental package on board the Polar-orbiting Operational Environmental Satellite (POES) spacecraft, which is described in more detail

below. However, there are numerous concerns and issues surrounding these experimental measurements, including contamination by low-energy protons [e.g., *Rodger et al*., 2010a; *Yando et al*., 2011], overwhelming contamination in solar proton events as well as inner radiation belt protons in the South Atlantic magnetic anomaly (SAMA) [*Rodger et al*., 2013], and the size of the pitch angle range sampled by the telescope relative to the bounce loss cone size [*Hargreaves et al*., 2010; *Rodger et al*., 2013].

In this paper we use ground-based subionospheric very low frequency (VLF) observations to determine EEP fluxes during the northern hemisphere summer months spanning 2005–2013. We undertake comparisons with the POES EEP measurements, as well as the whistler mode chorus intensities which may be driving the precipitation through wave-particle interactions. Our study builds on an earlier ground-based paper by *Clilverd et al*. [2010] by using a larger data set (November 2004–December 2013), a more sophisticated analysis of the subionospheric data, as well as multiple improvements to the modeling approach, including allowing for changing energy spectral gradients in the EEP and solar cycle changes in the ambient *D* region ionosphere. We also present some data quality checks undertaken on the AIMOS model output. We attempt to validate the model with our improving understanding of EEP from the MEPED/POES and Antarctic-Arctic Radiation-belt Dynamic Deposition VLF Atmospheric Research Konsortia (AARDDVARK) observations. This is the first attempt to validate AIMOS model outputs for electron energies greater than ~10 keV, which is necessary as the model is now being used to examine mesospheric EEP impacts by some authors [e.g., *Funke et al*., 2011].

2. Experimental Setup

2.1. AARDVARK Observations

Antarctic-Arctic Radiation-belt Dynamic Deposition VLF Atmospheric Research Konsortia (AARDDVARK) is a global network of radio wave receivers which monitor powerful narrowband VLF (very low frequency) transmitters. Subionospherically propagating VLF waves are used to monitor energetic electron precipitation (EEP) through changes in the ionization rates of the lower ionosphere (50–90 km). Excess ionization caused by EEP causes perturbations in the amplitude and phase of received VLF signals, which can be found through comparison with the quiet day propagation levels. Radio wave propagation modeling may then be used to determine the EEP fluxes required to cause the observed changes, following the techniques outlined in *Rodger et al*. [2012].

We primarily focus on the radio wave observations made by the two AARDDVARK receivers situated at Sodankylä (Sodankylä Geophysical Observatory (SGO)), Finland (67°13′N, 26°22′E; $L = 5.2$). These were an OmniPAL receiver (operational November 2004–April 2013 [*Dowden et al*., 1998]) and the newer UltraMSK receiver (operational April 2010 to present [*Clilverd et al*., 2009]). Both receivers monitor the minimum shift keying VLF transmissions from a communication station located in Cutler, Maine, USA (24.0 kHz, 44°35′N, 67°16′W; $L = 2.9$), which has the call sign NAA. The transatlantic path between NAA and SGO lies directly underneath the outer radiation belt ($L = 3 - 7$), such that the VLF transmissions along this path are directly influenced by outer radiation belt energetic electron precipitation. Figure 1 (left) presents a map showing the transmitter and receiver locations as well as the propagation great circle path. Lines of constant *L* are displayed to indicate the footprints of the outer radiation belt. The monthly averaged *Ap* values and sunspot number are displayed in Figure 1 (right), showing the entire time period considered. This gives an indication of the changing conditions across the ~9 year November 2004–December 2013 period, which spans most of a solar cycle.

AARDDVARK NAA median amplitude measurements at SGO with 1 min time resolution were constructed from the 0.2 s native resolution data. The measurements from the two independent receivers were combined together to provide a more continuous data set. By comparing the observations across the 3 years when the two receivers were operating simultaneously, we have been able to successfully combine the data sets, with the UltraMSK eventually replacing the OmniPAL after it suffered a terminal failure in mid-2013. This combination leads to our very long (>9 years) data set of 1 min resolution NAA-SGO amplitude measurements. A careful check was undertaken to remove any erroneous data associated with receiver or transmitter operational problems and correcting for some timing discrepancies. Figure 2 shows the 2859 days of NAA-SGO median amplitude observations after these checks (~327 days of erroneous OmniPAL data were removed and ~143 days of erroneous UltraMSK data). Distinct patterns are clearly visible in the amplitude data corresponding to seasonal and daily variations in the ionosphere, mostly due

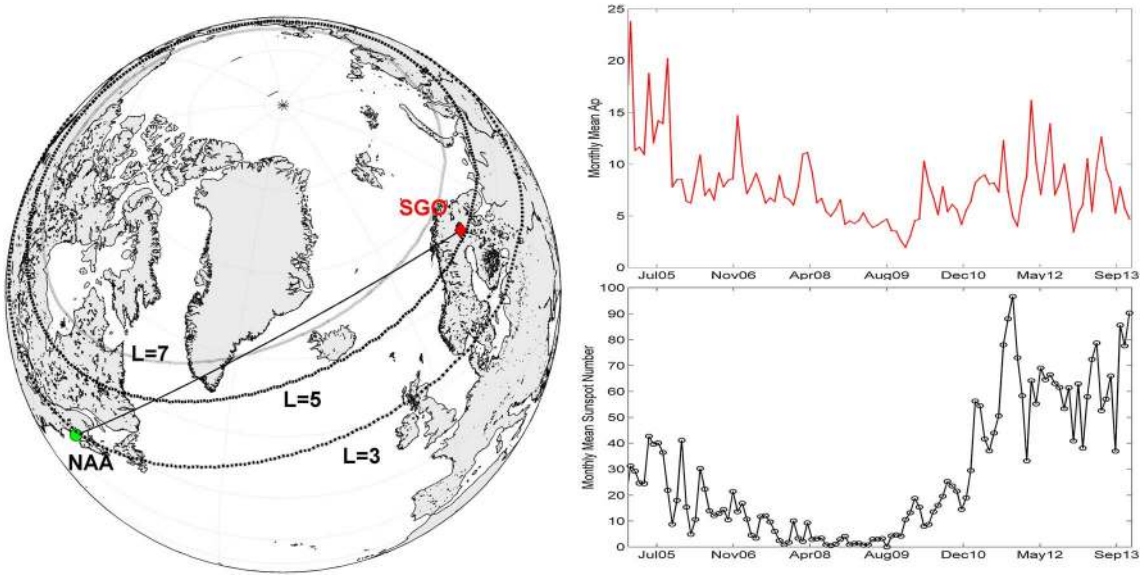

Figure 1. (left) Map of the subionospheric VLF propagation path from the NAA transmitter to the SGO receiver. The contours of constant *L* shell are shown indicating the atmospheric footprints of $L = 3$, 5, and 7. (upper right) Monthly average *Ap* value for the period of November 2004 to December 2013. (lower right) Monthly average sunspot number over the same time period.

to the changing solar zenith angles. One of the main features present in the data is the effect of sunrise (~08:00 UT) and sunset (~20:00 UT) on the path and the seasonal variation affecting the length of the sunlit period across the path. A deep minimum can be seen in the midday amplitude data during winter time in 2009–2010, corresponding to the period of solar minimum. This demonstrates the expected dependence of the ionospheric *D* region (and hence subionospheric propagation) on the changing solar cycle [*Thomson and Clilverd*, 2000].

The NAA-SGO subionospheric VLF path is affected by the impact of solar proton events on the *D* region along that path [*Rodger et al.*, 2006, 2007a]. Any attempt to monitor EEP using NAA-SGO subionospheric observations will potentially be confounded by the strong ionospheric response to solar protons; hence, we remove 144.8 days worth of 1 min amplitude observations from our analysis, leaving a total of 2714.6 days worth of observations remaining. Solar proton events were identified using the list provided by NOAA (available at http://www.swpc.noaa.gov/ftpdir/indices/SPE.txt), which provides the >10 MeV proton flux observed at geostationary orbit over the time period of 1976 to present. Note that a solar proton event in this list is defined as spanning the time from when the flux climbs above 10 pfu (where pfu is the proton flux unit (protons s^{-1} sr^{-1} cm^{-2} for >10 MeV protons measured at geostationary orbit)) to when the flux again falls below this value.

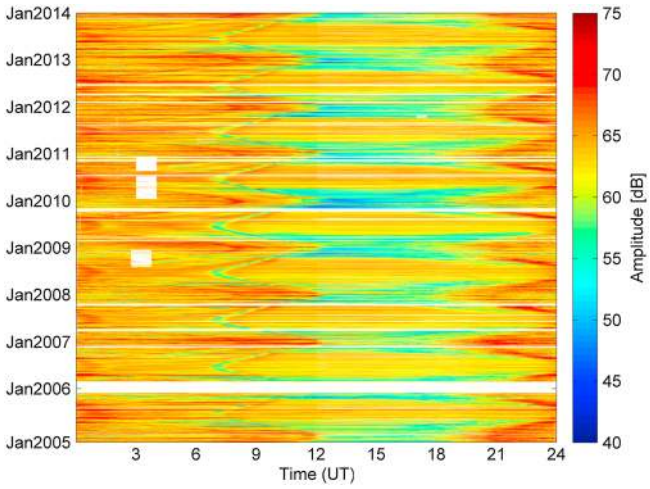

Figure 2. Slightly more than 9 years of 1 min resolution median amplitudes of the transmissions from NAA received at Sodankyla (SGO), Finland. The colors represent the amplitude of the received signal in decibel relative to an arbitrary reference level. The white regions correspond to either missing or removed (unreliable) data.

2.2. POES EEP Observations

The Polar-orbiting Operational Environmental Satellites (POESs) are low-altitude (~800–850 km) spacecraft with Sun-synchronous polar orbits with periods of ~100 min. Since 1998, the

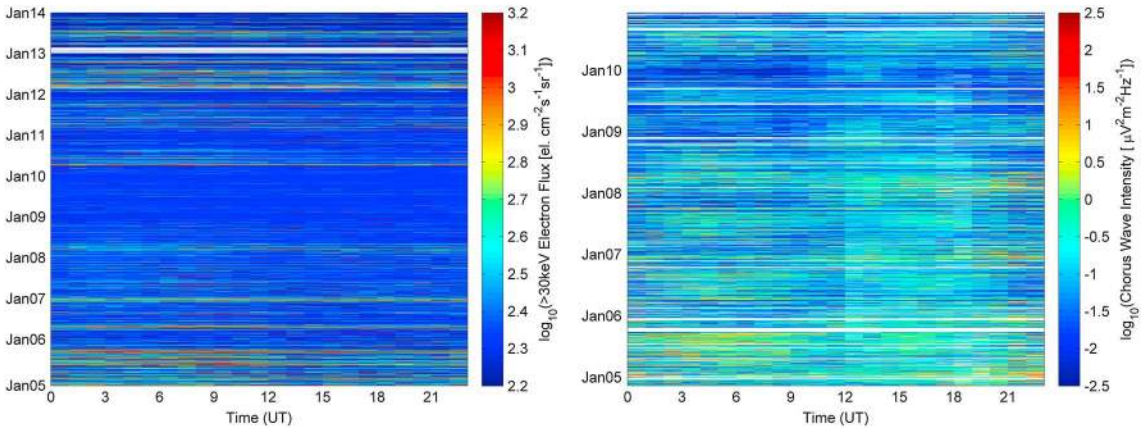

Figure 3. (left) Variation in the median hourly POES 0° >30 keV electron flux averaged across $L = 3 - 7$. The 0° electron telescope measures electrons deep inside the BLC. (right) Hourly median DEMETER observations of lower band chorus mode wave intensity averaged across $L = 3 - 7$, with no MLT restriction.

POES spacecraft have carried the second-generation SEM-2 [*Evans and Greer*, 2004], which measures energetic charged-particle fluxes using the Medium Energy Proton and Electron Detector. To date, seven POES spacecraft have operated the SEM-2 package in orbit (NOAA 15–19 and MetOp 1–2). The SEM-2 detectors include integral electron telescopes with energies of >30 keV (e1), >100 keV (e2), and >300 keV (e3), pointed in two directions. In this study we focus primarily upon the 0°-pointing detectors, as this primarily monitors deep inside the bounce loss cone (BLC) [*Rodger et al*., 2010a, Appendix A]. Previous studies have identified significant contamination in the electron channels by protons with energies of hundreds of keV [*Yando et al*., 2011], which are particularly significant during storm times. We correct this using a NOAA-developed algorithm as described in Appendix A of *Lam et al*. [2010] and recently validated by *Whittaker et al*. [2014]. We follow *Rodger et al*. [2013] and remove these periods using the MEPED P7 omnidirectional observations of >36 MeV protons. We first combine the POES-reported particle fluxes varying with International Geomagnetic Reference Field *L* and time, using 0.25 *L* and 15 min time resolution. Observations from inside and around the South Atlantic magnetic anomaly are excluded before the measurements are combined, although the P7 test to exclude solar proton events also suppresses all measurements in the SAMA region, where inner radiation belt protons swamp the electron detectors [*Rodger et al*., 2013]. The variation of the hourly outer belt >30 keV EEP fluxes is shown in Figure 3 (left). Note that in 2009, the POES EEP drops to very low precipitation levels (noise floor level). This time period spans an extended period of low solar activity, in which the trapped low Earth orbit relativistic electron fluxes reported by SAMPEX [*Russell et al*., 2010] and the geosynchronous GOES observations both fell to noise floor levels. Similar decreases in the POES-trapped relativistic electrons have been reported, which were noted as being "unprecedented in the ~14 years of SEM-2 observations" [*Cresswell-Moorcock et al*., 2013]. In the same time period, that study noted the outer belt >100 keV POES-trapped electron fluxes decreased by 1–1.5 orders of magnitude, recovering to the typical long-term average in 2010.

We fit a power law spectrum to the three 0° electron telescopes to obtain the energy spectral gradient (*k*) for the precipitating electrons; a recent comparison between the high-energy resolution DEMETER electron flux observations with POES has reported that power laws were accurate representations of the flux spectrum [*Whittaker et al*., 2013]. The resulting POES spectra are used in the modeling sections of the current study to help determine the EEP fluxes from the NAA-SGO AARDDVARK observations. The MEPED/POES >30 keV BLC fluxes will be later contrasted with the EEP fluxes reported from the AARDDVARK amplitude differences. At the same time, >100 keV (e2) and >300 keV (e3) EEP will also be taking place and reported by POES. However, we use the >30 keV (e1) for our comparisons as these fluxes are consistently larger and thus more likely to be above the MEPED/POES noise floor levels. Note that there is a strong correlation between the fluxes in e1, e2, and e3 (as discussed in section 5.2).

2.3. DEMETER Lower Band Chorus

As well as comparing the NAA-SGO EEP fluxes to the POES EEP measurements, we also investigate the connection to likely plasma wave drivers causing the EEP. We make use of observations from the ICE

(Instrument Champ Electrique) instrument on board the DEMETER spacecraft to examine this. The DEMETER satellite was launched in June 2004, flying at an altitude of 670 km (after 2005) in a Sun-synchronous orbit with an inclination of 98°. The ICE instrument provides continuous measurements of the power spectrum of one electric field component in the VLF band [*Berthelier et al*., 2006]. Here we make use of both survey and burst mode data of the electric field spectra recorded up to 20 kHz, with a frequency channel resolution of 19.25 Hz. We analyze ICE/DEMETER data up to early December 2010, shortly before the deorbiting of the satellite in March 2011. The high-time-resolution ICE/DEMETER data have been reprocessed to determine the hourly mean intensity of waves over $L = 3 - 7$ in the frequency band from 0.1 to 0.5 f_{ce}, where lower band chorus occurs. We combine both the "day" and "night" DEMETER observations; i.e., there is no restriction on magnetic local time (MLT), to produce the highest possible time resolution. Note that DEMETER has previously been used to study whistler mode chorus despite its comparatively low altitude [e.g., *Santolík et al*., 2006; *Zhima et al*., 2013]. Figure 3 (right) shows the variation in the observed median DEMETER lower band chorus wave power across the entire mission life. Once again, the solar minimum period in 2009 shows lower levels of chorus intensity, emphasizing the quietness of this time.

3. QDC Generation

The quiet day curve (QDC) describes the annual and daily background (which one might also term, "quiet" or "undisturbed") variation in the received VLF amplitude measurements. The received amplitudes of fixed frequency VLF transmissions vary in a constant manner during undisturbed conditions. Energetic electron precipitation (EEP) events can be detected as deviations from the subionospheric quiet day curve as a change in amplitude of the received signal relative to the QDC [*Rodger et al*., 2012; *Simon Wedlund et al*., 2014]. This is equivalent to the QDC approach used for riometers, which has become standard practice in that community.

For the NAA-SGO path, EEP causes changes in the *D* region electron density, which tends to lead to increases in the received amplitudes, such that the lowest amplitudes occur during the quietest times. This is most reliable for time periods when the NAA-SGO path is dominated by a sunlit ionosphere. The consistent amplitude increases during summertime *D* region perturbation times were identified by *Clilverd et al*. [2010], who exploited it to manually produce QDCs for three different UT time slices 02:00–03:00, 08:00–09:00, and 16:00–17:00 UT to determine the EEP magnitudes. In our study, we have also exploited the same behavior but developed an automatic process to produce QDCs for all UT times directly from the observed subionospheric VLF amplitudes. For each UT hour, we determine the mean and standard deviation of the experimentally observed amplitude values. The QDC was generated by subtracting 2 standard deviations from the mean and then smoothed with a 19 day sliding average. We investigated a range of possible averaging windows, from 3 to 51 days, and concluded that 19 days performed the best, giving a smoothly varying QDC without rounding away the large modal features present. Figure 4 (left) shows the QDCs determined for 02:00–03:00, 08:00–09:00, and 16:00–17:00 UT for the 2005 observations, along with the QDCs for the same 1 h time period from *Clilverd et al*. [2010]. Our approach leads to a QDC that follows the lower edge of the amplitude data (blue line) and has similar shape to that given by *Clilverd et al*. [2010] for the 2005 QDCs (red line) determined from their somewhat naïve "straight line" minimum approach.

Figure 4 (right) shows the QDC generated at 1 h time resolution across the entire ~9 year period of experimental observations. A deep midday minimum can be seen in 2009/2010 during the winter, i.e., during the solar minimum. However, the opposite behavior can be seen for the noontime summer amplitudes; the QDC amplitude for solar minimum (2009/2010) is ~2.3 dB higher than seen during solar maximum in 2005. This is addressed further in section 4.1.

4. Modeling of EEP Impact on VLF Propagation

In order to interpret the significance of observed changes in a received VLF signal, it is necessary to make use of a propagation model. This allows one to link the properties of the ionization changes occurring around the upper boundary of the Earth's ionosphere waveguide (i.e., the lower part of the *D* region) with the magnitude of the changes in the VLF transmissions. Here we use the U.S. Navy Long Wave Propagation Code (LWPC) [*Ferguson and Snyder*, 1990]. LWPC models the propagation of fixed-frequency VLF waves from a transmitter to a receiver, calculating the received amplitude and phase. The great circle path between these two points is broken into a series of segments, accounting for changes in geophysical

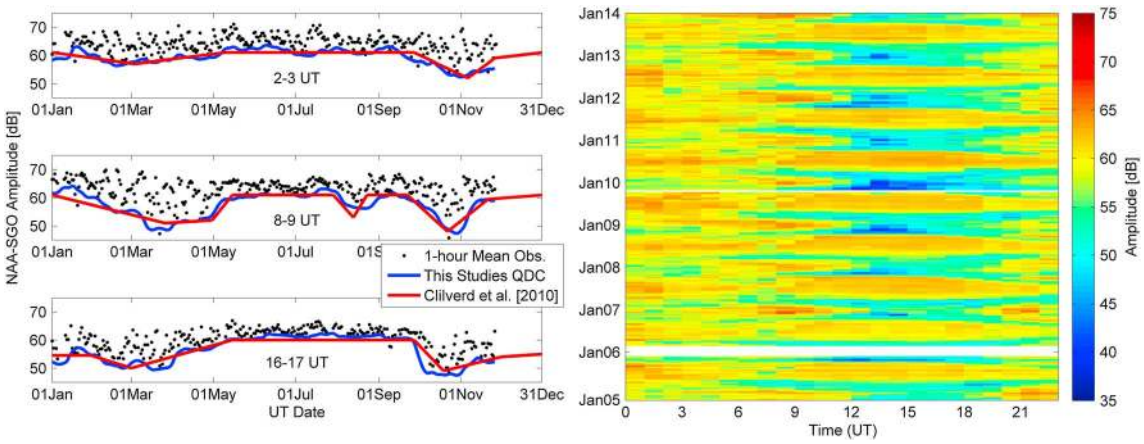

Figure 4. (left) Examples of QDCs generated in this study (blue) to represent the 2005 amplitude observations at 02:00–03:00, 08:00–09:00, and 16:00–17:00 UT. The QDCs for the same time spans presented in *Clilverd et al.* [2010] are shown in red for comparison. The new method follows the lower edge of the amplitudes more closely but is similar to that put forward in the earlier study. Note the large data gap in December 2005, which is also seen in Figure 2. (right) The QDC generated across our entire ~9 year time period.

parameters along the path to be allowed for. For each segment, the program takes into account the variations in ground conductivity, dielectric constant, orientation of the geomagnetic field with respect to the path, solar zenith angle, and the electron density profile (i.e., electrons m^{-3}).

The electron density profile is varied by forcing the atmosphere with EEP from above. A short description of the modeling process is given below; for a full description, see *Rodger et al.* [2012]. A series of coupled models are used to determine the equilibrium electron number density which will subsequently be fed into LWPC: the ionization rates due to the EEP [*Rees*, 1989; *Goldberg et al.*, 1984], the background neutral atmosphere [*Picone et al.*, 2002], and the equilibrium electron number density in the lower ionosphere [*Rodger et al.*, 1998, 2007a, 2012]. The electron density profiles are determined for a range of precipitation flux magnitudes and power law energy spectral gradients ranging from +0.5 to −5 with 0.5 steps. We assume that EEP spans the energy range of 10 keV to 3 MeV but report the >30 keV flux magnitudes to allow direct comparison with the POES observations. The electron density profiles are then used as inputs into the LWPC subionospheric propagation model and applied uniformly along the path. Thus, we model the effect of electron precipitation on the VLF amplitudes from NAA received at Sodankylä.

4.1. Incorporating the *D* Region Yearly Variability

For undisturbed time periods, the *D* region electron density altitude profile is often expressed through a Wait ionosphere, defined in terms of a sharpness parameter β and a reference height H' [*Wait and Spies*, 1964], with the electron number density increasing exponentially with altitude. *Clilverd et al.*'s [2010] study of the NAA-SGO path used fixed ambient daytime ionosphere parameters ($\beta = 0.3\ km^{-1}$, $H' = 74$ km) consistent with the nondisturbed amplitudes of NAA experimentally observed at SGO for 2005. As seen in Figure 4, there is evidence of changes in the nondisturbed *D* region across the solar cycle. We took the mean daytime summer (May–July) amplitude difference for each year and compared those values to that determined from 2005. We observed that the differences in QDC noontime (16:00–17:00 UT) amplitudes gradually increase from the relatively high solar activity in 2005 to solar minimum (2009/2010). These changes can be seen in Figure 4 (right) and in Figure 5. The maximum variation is ~2.5 dB, after which the amplitude difference decreases as the solar cycle advances toward solar maximum conditions. These changing QDC noontime (16:00–17:00 UT) amplitude values were used to determine the variation in the Wait ionospheric β parameter required to represent the solar cycle variations in the *D* region from 2005 to 2013. This was undertaken using LWPC with quiet (i.e., zero EEP) propagation modeling. We follow *Clilverd et al.* [2010] and use a β value of $0.3\ km^{-1}$ for 2005, which increases to produce the observed increasing QDC amplitudes (Figure 4), such that for solar minimum conditions, β has evolved to ~$0.42\ km^{-1}$ (Figure 5). Note the smooth and consistent variation in β shown in Figure 5 with the progression of the solar cycle. H' was held constant here throughout the solar cycle, partly because *McRae and Thomson* [2000] reported that H' changed

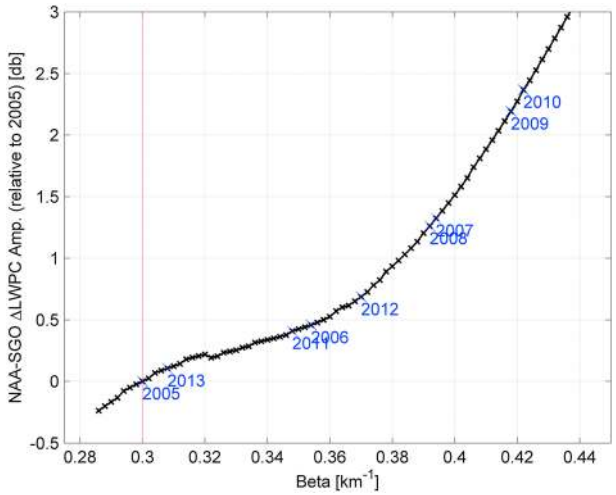

Figure 5. Change of the Wait ionosphere β parameter used in the LWPC modeling determined from the observed QDC noontime amplitude changes across the solar cycle.

by only ~1 km from solar maximum to solar minimum at midlatitudes (no appropriate high-latitude measurements are available to the best of our knowledge) and partly because LWPC modeling (not shown) indicates that the amplitude for the NAA-SGO path was only weakly dependent upon *H′*. This adjusted beta value is then used in LWPC to produce separate modeling of the expected impact of EEP on the NAA-SGO amplitudes for each year.

4.2. Incorporating EEP Energy Spectral Variability

The energy spectra of precipitating energetic electrons are well represented by a power law [*Whittaker et al.*, 2013]. The previous study into EEP monitored using observations from the NAA-SGO path by *Clilverd et al.* [2010] used modeling based on a fixed power law with a gradient of $k = -2$. We remove this limitation by using a variable energy spectrum in our modeling of how the EEP impacts the ionosphere and modified the VLF propagation. The energy spectral gradient of the precipitating fluxes was varied from $k = -5$ to 0.5 in steps of 0.5. The differing spectral gradients lead to significantly different amplitude changes for a given EEP flux magnitude and ambient ionospheric profile. Examples of this are shown in Figure 6, which presents the LWPC-predicted amplitudes for a range of EEP magnitudes and spectral gradients for 2006 (Figure 6, left) and 2010 (Figure 6, right).

Recently, the EEP power law spectral gradient was determined directly from AARDDVARK measurements made in Canada during a series of geomagnetic storms [*Simon Wedlund et al.*, 2014]. This relied upon simultaneous amplitude perturbation observations on two different AARDDVARK paths, which are likely to sense similar EEP activity, along with LWPC modeling using a range of spectral gradients which were combined to determine the most likely EEP energy spectral gradients occurring for any given time and day. We are unable to apply this approach in the current study as we do not have an appropriate second path. However, *Simon Wedlund et al.*'s [2014] study found good agreement between the POES and AARDDVARK-determined gradients, giving us additional confidence in the use of the POES-fitted energy gradients as we describe in the following section.

5. AARDDVARK-Extracted EEP

We now combine the AARDDVARK experimentally observed NAA-SGO amplitudes with the LWPC modeling described above to extract EEP flux magnitudes from the VLF perturbations. The 1 min observations are averaged to produce hourly mean NAA-SGO amplitude leading to 2762.1 days worth of hourly values—note that the ~1.7% increase in the days worth of data is caused by the averaging of partial hours worth of 1 min data being combined to produce the hourly average. The amplitude QDCs seen in Figure 4 (right) are subtracted from the hourly average amplitude values to produce 2762.1 days worth of amplitude perturbations.

In order to use the LWPC modeling results (e.g., Figure 6), an appropriate EEP power law value is required. We use 1 h resolution POES satellite data to fit a power law to the three EEP electron flux energy ranges and thus produce a dynamic energy spectral gradient for the precipitating electron population. The changes in amplitude results produced by the LWPC modeling for the specific power law value are then linearly interpolated to produce the variation in amplitude perturbations with $\log_{10}$ (flux magnitude) for a specific power law gradient. An EEP flux magnitude may be obtained by matching the observed NAA-SGO amplitude with the modeled amplitude; the latter of which may correspond to one or more EEP values. In situations where more than one solution exists, the EEP magnitude closest to the previous hour's value is selected. The

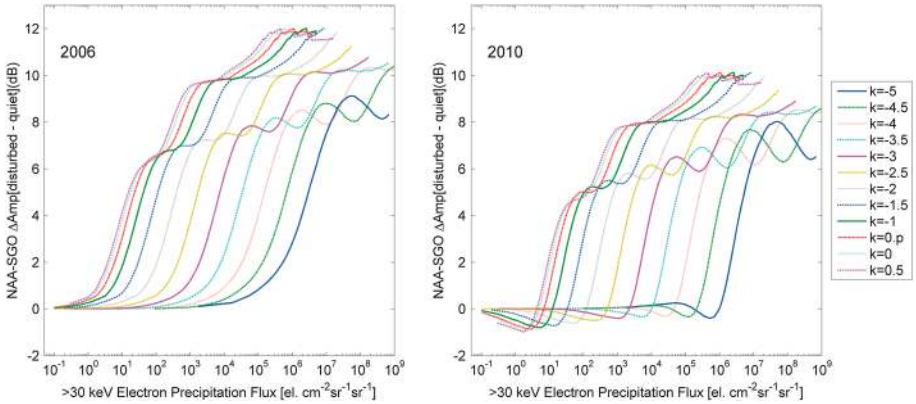

Figure 6. Daytime LWPC modeling of the amplitude changes due to EEP fluxes for the path NAA-SGO for (left) 2006 and (right) 2010. The energy spectra of the precipitating elections are specified using a power law which is varied through the *k* parameter. The modeling used the updated Wait ionosphere parameters for each year, shown in Figure 5.

observed amplitude values larger than the maximum modeled values are excluded. This affects ~108.4 days worth of perturbations, of which only ~1.5 days worth fall in the summer months.

At this point, our modeling and QDC determination approaches are only reliable when the NAA-SGO path is dominated by solar photoionization, i.e., the summer period. *Clilverd et al*. [2010] suggested that the approach worked for the middle ~150 days of the year, roughly from 10 April to early September. In the current study, we take a more conservative view and restrict ourselves to observations occurring each year in the 92 day "summer" period from 1 May to 1 August. This produces 693.25 days worth of 1 h resolution EEP values, which appear well behaved. Examples of the AARDDVARK-extracted EEP are seen in Figure 7 (black lines).

5.1. Comparison With POES-EEP

To check the validity of our EEP flux extraction process, we compare the AARDDVARK-reported fluxes with the >30 keV EEP measurements made by the POES spacecraft. Figure 7 shows the variation of the AARDDVARK-extracted EEP fluxes (black lines) for the northern hemisphere summer periods during 2005–2009. The corresponding >30 keV POES EEP observations are shown in Figure 7 by the red line. The AARDDVARK-extracted EEP fluxes are almost independent of the POES measurements, other than the inclusion of the POES-reported power law gradients. Despite being largely independent EEP measures, both data sets show that the EEP in the years closer to solar maximum (2005–2006) were considerably more active than those near solar minimum (2009), which was very quiet. As mentioned above, during solar proton events, our ability to detect EEP is masked. In both middle and late July 2005, solar proton events occurred, and as such, there is no AARDDVARK-extracted EEP for that time period in Figure 7 (top).

Figure 7 demonstrates that during large precipitation events, both the AARDDVARK and POES EEP fluxes report similar maximum magnitudes. It has been argued previously that the MEPED/POES BLC fluxes may be underreported for weak precipitation events [*Hargreaves et al*., 2010; *Rodger et al*., 2013], where the loss cone is not filled. In contrast, during strong EEP events likely associated with strong diffusion [*Rodger et al*., 2013; *Clilverd et al*., 2014], the MEPED/POES BLC fluxes are expected to be more accurate representations of the precipitating striking the atmosphere; as such, one would hope for good agreement between the AARDDVARK and MEPED/POES fluxes at these times, as seen in Figure 7. The small size of the MEPED/POES telescope detector translates into rather low sensitivity at smaller flux magnitudes [*Yando et al*., 2011] reflected by their noise floor level of ~150 el $cm^{-2}\,s^{-1}\,sr^{-1}$ (Figure 3, left). This is also seen in Figure 7, where the MEPED/POES >30 keV EEP flux during quiet periods is constantly ~10^2 el $cm^{-2}\,s^{-1}\,sr^{-1}$. The AARDDVARK-extracted fluxes have a noise floor value which is 10–50 times lower than the MEPED/POES instrument, emphasizing that the true flux into the atmosphere during quiet periods is much lower than suggested from the satellite observations. This is particularly clear in the 2009 panel of Figure 7, where low-intensity EEP fluxes occur in the AARDDVARK-extracted data but are poorly represented in the MEPED/POES fluxes.

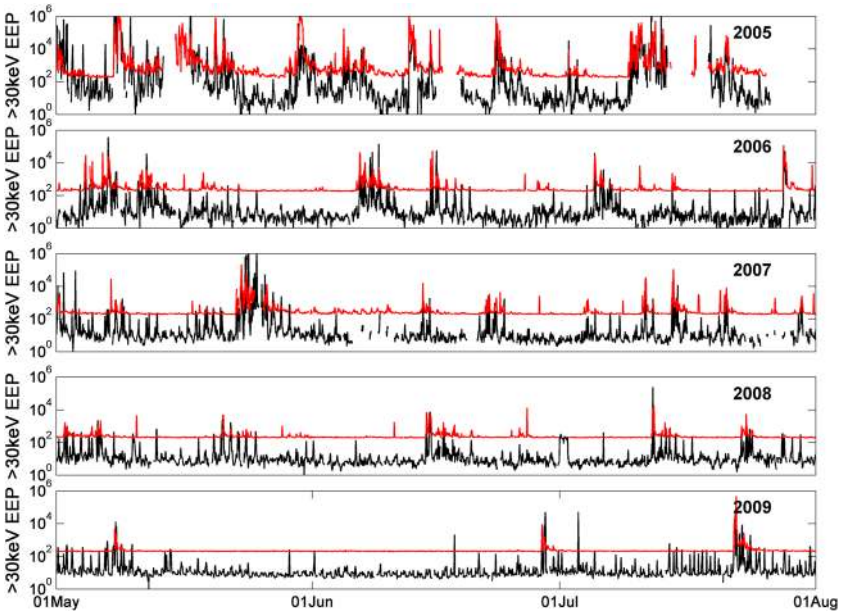

Figure 7. Comparison between the NAA-SGO-determined EEP flux magnitudes (black) and the MEPED/POES >30 keV electron fluxes (red) during the summer months over 5 years. In all cases, the fluxes are shown with units of $cm^{-2}\,s^{-1}\,sr^{-1}$. The change in activity level between solar minimum (~2009) and near solar maximum (2005) can easily be recognized.

5.2. Estimation of Uncertainties

We have also tested the sensitivity of our AARDDVARK-extracted EEP magnitudes to uncertainties in the AARDDVARK amplitudes. Uncertainties in subionospheric VLF QDC will depend upon the time of day, the receiver design, and the background noise levels. We follow an earlier study which concluded that there was a ±0.3 dB amplitude uncertainty as a result of removing the subionospheric QDC at noontime [*Rodger et al.*, 2007a]. The EEP extraction process described above is rerun for amplitude differences which are 0.3 dB higher and lower than the observed amplitude perturbation in order to test the sensitivity. As one might expect, during quiet times, the uncertainty levels in the >30 keV flux levels are low (~1–2 el $cm^{-2}\,s^{-1}\,sr^{-1}$), but during high EEP periods, the uncertainty levels in the >30 keV flux levels are considerably larger (~10^4 el $cm^{-2}\,s^{-1}\,sr^{-1}$). When comparing these values with the observed EEP flux magnitudes, we find that the uncertainties vary from ~10 to 1000% and are typically ~20%. However, this is dominated by the quiet (low flux) periods. During high EEP periods, the uncertainties introduced by the amplitude error are a few times larger (i.e., 200–500%).

We have also tested the sensitivity of our AARDDVARK-extracted EEP magnitudes to uncertainties in the POES-fitted energy spectral gradients. We assumed that the e1, e2, and e3 MEPED/POES EEP flux values had an uncertainty of 50%. We changed the 2005 fluxes by a random amount up to this uncertainty level but also required that the modified flux in e1 was greater than or equal to that for e2 and that the modified e2 flux was greater than or equal to that for e3. We then undertook the spectral fitting as outlined in section 2.2. This was repeated 20 times to produce an estimate of the error in the spectral gradients. While our choice of 50% for the error value is fairly arbitrary, it is similar to the ~30% uncertainty estimated as the possible error in the earlier SEM-1 electron flux estimates [*Tan et al.*, 2007]. The average uncertainty in the k value was 0.51. We then repeated the process of determining the EEP magnitudes from AARDDVARK data using the k values modified by the uncertainties found for each 1 h period. The average change in magnitude is ~1.8. The EEP flux magnitude changes are not particularly large, with the effect being less significant than allowing k to vary (as discussed in section 7.1).

An important assumption in our approach is to assume that the energy spectrum of the EEP is well represented by power law spanning medium and relativistic energies. There is a high correlation between the three electron energy channels reported by the POES spacecraft. The MEPED/POES EEP fluxes described in section 2.2 are strongly correlated with one another. After removing solar proton events and data gaps, we

find that the correlation of the $\log_{10}$ (flux) of the e1 and e2 channels across our L shell range is 0.99; for e2 and e3, this value is 0.987; and for e1 and e3, the correlation value is 0.970, although these high-correlation values will be strongly influenced by the noise floor. As noted in section 2.2, we take some confidence in the use of the power law to describe the energy spectra of the EEP from the high-energy resolution of the DEMETER satellite. This spacecraft primarily measured in the drift loss cone and hence for pitch angles only slightly above the BLC. The recent *Whittaker et al.* [2013, 2014] studies found that the drift loss cone observations by DEMETER, and the POES telescopes, were best fitted by a power law. This held for energies spanning medium and relativistic energies (up to ~1.2 MeV). Whistler mode waves, such as chorus, can pitch angle scatter electrons into the BLC over a very wide energy range. For example, recent simulations of chorus-driven precipitation reported electrons spanning a few keV to several MeV [*Saito et al.*, 2012], with a lower limit of ~10 keV for $L = 5$.

We note that there is evidence that power laws may not best represent the EEP energy spectrum for relativistic energies. SAMPEX observations of drift loss cone and bounce loss cone relativistic electron (0.5–5.66 MeV) precipitation seem to have been well represented by an exponential dependence [*Tu et al.*, 2010]. The Taranis mission [*Pincon et al.*, 2011] will provide DEMETER-like high-energy resolution electron flux measurements for both the drift loss cone and BLC and may be able to clarify this issue.

5.3. Comparison With DEMETER Chorus Waves

Lower band chorus waves are known to drive electron precipitation via resonant interactions [*Lorentzen et al.*, 2001; *Horne et al.*, 2003], where the rate of precipitation scales in direct proportion to the power spectral intensity of resonant waves [*Millan and Thorne*, 2007]. To test this, we have contrasted the lower band chorus wave intensity detected by DEMETER (Figure 3, right) with our AARDDVARK-extracted EEP fluxes. Figure 8 shows the NAA-SGO >30 keV EEP fluxes (black line) and the DEMETER lower band chorus intensity (blue line) for 2005, 2006, and 2009. In both cases, the EEP flux and chorus intensities are medians limited to 02:00–08:00 UT (corresponding to ~22:00–12:00 MLT along the great circle path), for which dawn chorus activity should be present.

This figure indicates that there is a reasonable correlation "by eye" between the EEP flux and the DEMETER chorus intensity, even during the very quiet 2009 period. After removing solar proton events and data gaps, we find that the correlation between the EEP flux and the DEMETER chorus intensity is 0.33, which is a modest-moderate level of correlation. It is often assumed that whistler mode chorus waves are the dominant cause of energetic electron precipitation outside of the plasmapause. Our observations provide some support for this assumption, which is backed by published theory and wave observations. Recently MEPED/POES >30 keV EEP observations were successfully used to predict chorus occurrence, validated by observations from the Van Allan Probes [*Li et al.*, 2013]. This approach is now being used to infer the chorus wave intensity and construct its global distribution directly from POES observations [*Ni et al.*, 2014] rather than relying on statistical models of wave occurrence.

6. Examination of the AIMOS Model

As part of the Quantifying Hemispheric Differences in Particle Forcing Effects on Stratospheric Ozone international team project hosted by the Swiss International Space Science Institute, an attempt was made to validate the precipitation-driven ionization rates reported by the AIMOS model [*Wissing and Kallenrode*, 2009]. AIMOS combines particle observations from low Earth POES and geostationary orbiting spacecraft with geomagnetic observations to provide 3-D numerical model of atmospheric ionization due to precipitating particles with high spatial resolution. Part of the validation effort involves comparison with ground-based radio wave observations, the initial stages of which have been reported elsewhere [*Rodger et al.*, 2014] and are being considered for a future detailed publication. Here we restrict ourselves to reporting on some issues in the AIMOS ionization rates which were identified in the initial data quality checks. We made use of AIMOS v1.2 which has been extensively used to describe the particle forcing during solar proton events and geomagnetic storms [e.g., *Funke et al.*, 2011] and has been validated for thermospheric altitudes [*Wissing et al.*, 2011] but not below. AIMOS provides ionization rate profiles for a given location and time range, with separate rates produced caused by the precipitation of protons, electrons, and alpha particles.

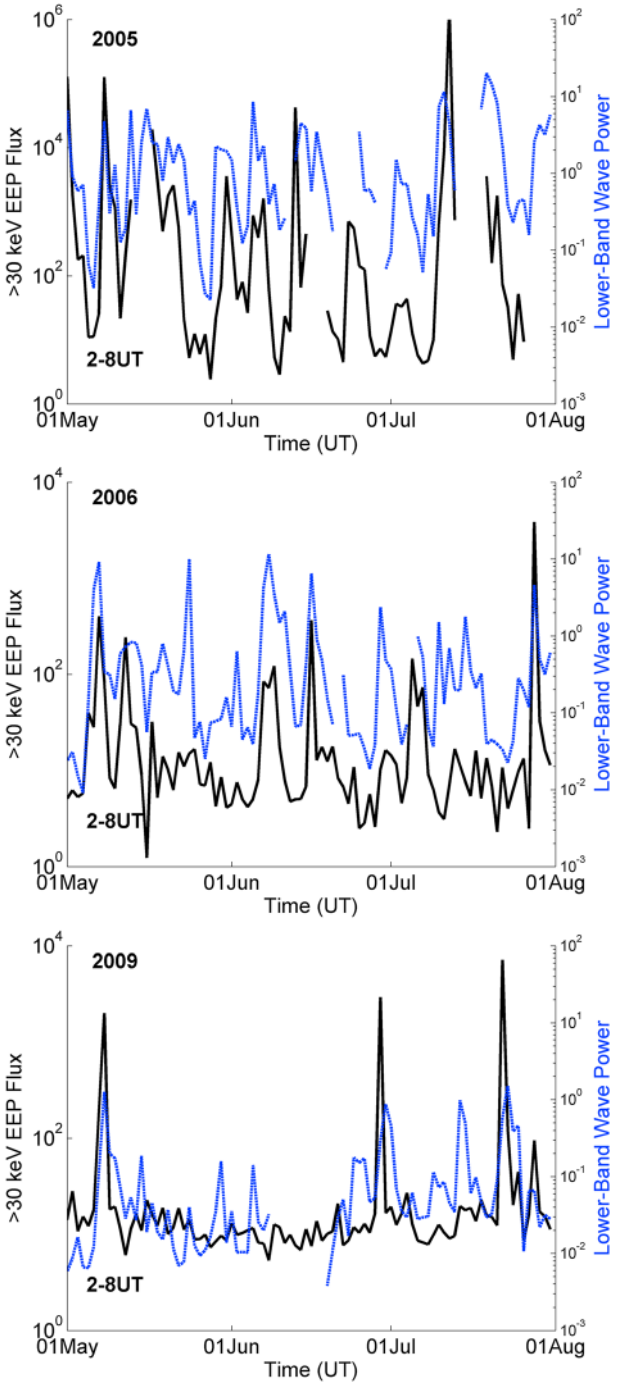

Figure 8. The variation in the NAA-SGO-determined EEP flux magnitudes (black line) contrasted with the varying lower band chorus wave intensity (blue line) observed from the DEMETER satellite. In both cases, the median over 02:00–08:00 UT is taken for each year.

Initial data quality checks identified numerous issues with the ionization rates from AIMOS v1.2, indicating that great care must be taken when drawing conclusions from studies using these models. We provide a summary of areas of concern below:

1. It has long been recognized that the MEPED/POES electron detectors suffer overwhelming contamination during solar proton events [*Evans and Greer*, 2004]. However, AIMOS v1.2 clearly includes these electron observations during solar proton events, leading to highly unrealistic electron ionization rates inconsistent with experimental observations [e.g., *Funke et al.*, 2011]. Figure 9 (top) shows the electron precipitation-produced ionization rates for 3 months in 2006–2007 for the path from NAA to SGO. Here the blue line overplotted on the ionization rates represents the GOES-reported >10 MeV proton flux (ranging from ~0.2 $cm^{-2}\,s^{-1}\,sr^{-1}$ to $1.95\times10^{3}\,cm^{-2}\,s^{-1}\,sr^{-1}$); a solar proton event occurred beginning on 5 December 2006. The overplotted lower black line shows the variation in the *Kp* geomagnetic index (which ranges from 0 to 8.3). During the December 2006 solar proton event, the ionization rates for proton precipitation-produced ionization (from 50 to 90 km altitudes) increase by 4–5 orders of magnitude (not shown). At the same time, the ionization rates reported by AIMOS due to electrons also increase by ~4–5 orders of magnitude, as shown in Figure 9 (top). There is no evidence for this electron precipitation outside of the contaminated POES observations.
   It is also well known that the MEPED/POES electron detectors suffer contamination from protons of ~100 keV at high latitudes [*Evans and Greer*, 2004; *Yando et al.*, 2011]. *Rodger et al.* [2010a] found that as much as ~42% of the 0° telescope >30 keV electron observations from MEPED were contaminated by such protons in the energy range, although the situation was less marked for the 90° telescope (3.5%). The existing algorithms to correct for proton contamination have not been applied in AIMOS v1.2.
2. During a data quality test, we examined the ionization rates near the geomagnetic equator above Fiji (18.2°S, 178.5°E; $L = 1.2$), where one would expect no particle input. During the December 2006 solar

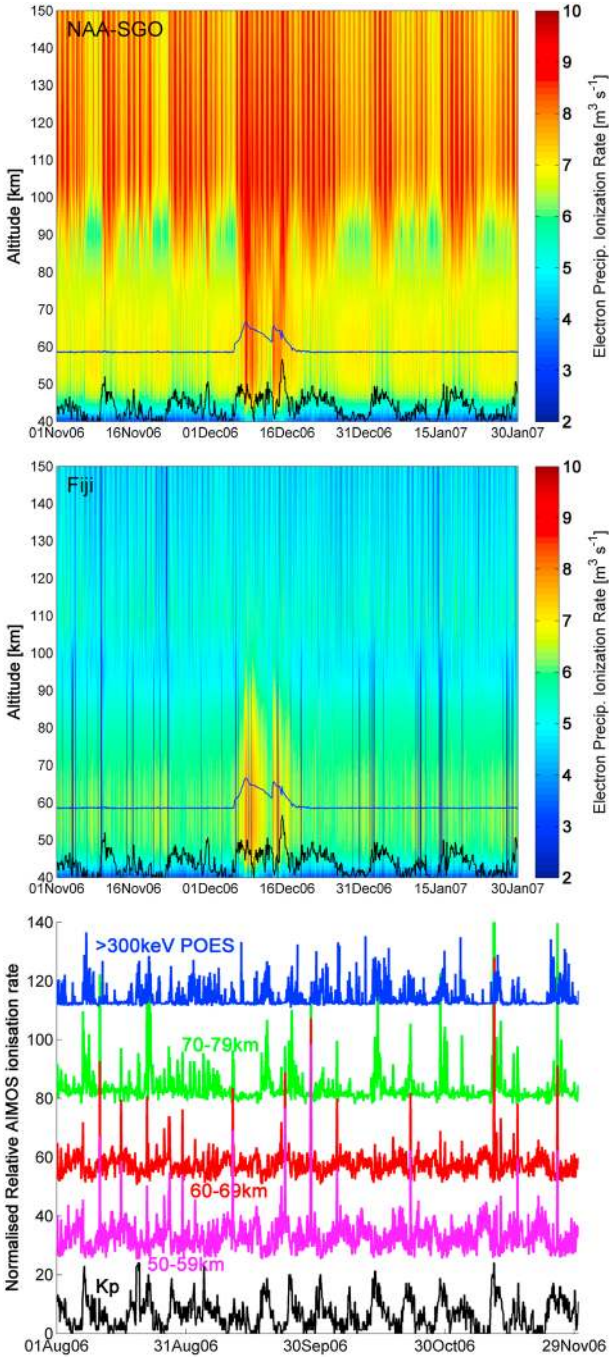

Figure 9. Ionization rates ostensibly due to electron precipitation reported by the AIMOS v1.2 model. (top) The rates for the NAA to SGO path. The black line shows the variability in the *Kp* geomagnetic index, and the blue line shows the GOES >10 MeV proton flux variation. (middle) The ionization rates above Fiji in the same format as the panel above. (bottom) The normalized variation in the AIMOS ionization rates for a range of mesospheric altitudes, with the >300 keV precipitating flux from POES EEP variation shown by the blue line and the *Kp* variation by the black line. Note that the Figure 9 (bottom) shows a different time range than Figure 9 (top and middle).

proton event, a 2 orders of magnitude increase in proton-produced ionization rates are reported above ~70 km altitude (not shown) by AIMOS, and at the same time, AIMOS reports a 2–3 orders of magnitude increase in electron-produced ionization rates for altitudes as low as ~45 km. This is seen in Figure 9 (middle), which is otherwise in the same format as the panel above. Solar protons cannot penetrate to these geomagnetic latitudes [*Rodger et al*., 2006] and are not seen in the MEPED/POES data above Fiji. Such protons are not visible in the data until the satellites are located more than 30° poleward of Fiji, indicating that the polar latitude observations are being incorrectly mapped into middle and low latitudes. Serious issues exist around the latitudinal binning of the satellite data to produce the precipitation input.

3. Figure 9 (bottom) shows the variation in AIMOS v1.2-reported EEP-produced ionization rates for the path from NAA to SGO for 4 months in late 2006 and a selection of mesospheric altitude ranges. This time range was selected to ensure that no solar proton event occurred. The ionization rates are normalized and shifted along the *y* axis to provide easy comparison. Here the black line shows the variation in the *Kp* geomagnetic index (which ranges from 0 to 6), and the blue line is the changing flux of MEPED/POES >300 keV precipitating electrons (which ranges from ~145 to ~6×10^3 cm^{-2} s^{-1} sr^{-1}). Note that electrons with energies above 300 keV should deposit the majority of their energy below ~75 km [e.g., *Turunen et al*., 2009]. There is a strong correlation between increases in geomagnetic activity and increases in >300 keV EEP, as expected. However, in the altitude ranges of 50–59 km and 60–69 km, there is a clear anticorrelation between the ionization rates, >300 keV EEP magnitude, and geomagnetic activity and a correlation between the rates and EEP flux in the 70–79 km altitude range. Examination of Figure 9 (top) shows that AIMOS v1.2-reported ionization rates above ~80 km increase during

geomagnetic disturbances, but the opposite occurs below ~75 km. For these lower altitudes, the ionization rates move from a quasi-constant value of ~10^7–10^8 to ~10^5–10^6 el m^{-3} during storms, i.e., a significant decrease in the ionization rates rather than an increase as expected from the experimental observations shown in Figures 7 and 8 and indeed in the relevant POES data itself shown in Figure 9 (bottom). We speculate that this is due to incorrect fitting of the EEP energy spectra in the AIMOS model.

4. As noted above (section 5.1), the MEPED/POES data are comparatively insensitive, with a noise floor at a rather high flux value (~10^2 el cm^{-2} s^{-1} sr^{-1}). The AIMOS v1.2 model includes the MEPED/POES noise floor data as if they are real precipitating elections, leading to the large quiet time mesospheric ionization rates seen in Figure 9 (top). This panel indicates quiet time rates outside of the SPE period of ~10^6–10^7 el m^{-3} s^{-1} at ~50–75 km altitude. In contrast, the background ionization rates in this altitude range are expected to be dominated by the effect of Lyman α and galactic cosmic rays with rate values of ~10^5–10^6 el m^{-3} s^{-1} [e.g., *Friedrich et al*., 1998, Figure 1; *Rodger et al*., 2007b, Figures 3 and 4]. Fluxes at the MEPED/POES noise floor level are sufficiently high to produce an ~4 times increase in the noontime electron number density at ~75 km altitude (not shown).

There are clearly numerous serious data quality problems in the AIMOS model outputs at altitudes of 60–80 km. Some of these appear to be due to contamination issues in the input data (e.g., MEPED/POES proton contamination); others are clearly inherent to the model. The validity of modeling studies making use of AIMOS v1.2 is questionable, and great care must be taken when considering the conclusions of such studies. To summarize, the AIMOS v1.2 ionization rates are unlikely to be accurate in the mesosphere and upper stratosphere during geomagnetically quiet times (when EEP levels are low), for middle and low latitudes, during solar proton events, or during geomagnetic storms (when there are high levels of EEP).

7. Discussion

7.1. Comparison With *Clilverd et al*. [2010]

Our study has introduced a number of improvements to the analysis and modeling relative to the original *Clilverd et al*. [2010]. In particular, we have used a more advanced *D* region model for calculating the equilibrium electron number density using *Rodger et al*. [2012] rather than *Rodger et al*. [2007a], improved on the data analysis so our QDC is not as simplistic, and allowed for the EEP energy spectra to change. We discuss the significance of each of these in turn.

The equilibrium electron number density is calculated from the ionization rate along with attachment and recombination rates. In *Clilverd et al*.'s [2010] study, these were from *Rodger et al*. [2007a], while we have used those from *Rodger et al*. [2012], which were found to be more broadly representative. This leads to a decrease in the EEP fluxes, with the typical >30 keV EEP flux magnitudes being ~0.55 of those reported by *Clilverd et al*. [2010].

The data-derived QDC is similar but not identical to that determined by *Clilverd et al*. [2010], as shown in our Figure 4. Our changing QDC produces both increases and decreases in the EEP magnitude relative to the earlier *Clilverd et al*.'s [2010] study. On average, the typical >30 keV EEP flux magnitudes produced by varying the QDC are ~0.51 of those reported by *Clilverd et al*. [2010].

The most significant driver for flux magnitude differences between the current study and the earlier *Clilverd et al*.'s [2010] work comes from allowing the energy spectral gradient of the precipitating fluxes to vary rather than holding it at a constant value of −2. During quiet times, the energy spectral gradient has values from about −1 to 0, leading to significant overestimates of the flux magnitude when a constant −2 gradient value is taken. In contrast, for storm times, the energy spectral gradient has values from −4 to −2, and the fixed-case modeling can suggest 1–2 orders of magnitude EEP lower magnitudes. On average, the typical >30 keV EEP flux magnitudes for a fixed $k = -2$ gradient value are ~14 times larger than for a varying gradient. Clearly, it is highly important to include the effect of varying energy spectral gradients where possible.

7.2. Application in Chemistry-Climate Models

As noted in the Introduction, there is growing interest in a broad scientific community into the impact of EEP upon polar atmospheric chemistry and the potential link to climate. This interest is driving researchers toward

incorporating EEP into chemistry-climate models to better represent the polar system and to test the overall significance. Due to previous scientific efforts, different examples of intense particle precipitation, for example solar proton events, can already be included in chemistry-climate models [e.g., *Jackman et al*., 2009]. Our current study, along with some of our previous papers, suggests that it is possible to accurately describe EEP using MEPED/POES observations for fairly strong events, assuming that sufficient care is taken with the data processing. The question of what to do when MEPED/POES reports fluxes near the instrumental noise floor remains. Our initial recommendation would be to set the EEP magnitude at those times to zero, taking a conservative view. We suggest that sensitivity tests using chemistry-climate models as to the significance of EEP fluxes below this noise floor value should be undertaken to determine whether setting those periods to zero is too harsh a condition or not.

We believe that the AARDDVARK-extracted EEP fluxes produced in the current study could be used for an initial test into the significance of EEP in chemistry-climate models and to examine the ability of these fluxes to reproduce the observed ozone signatures during EEP events [e.g., *Andersson et al*., 2014b]. However, further work in this area is needed before truly realistic global EEP fluxes can be incorporated into chemistry-climate models. We suggest that future focus on longitudinal/MLT variability and increased energy resolution (and in particular correlations or otherwise between medium and relativistic energy electron precipitation) would be of value in this research area.

In addition, a significant requirement from the atmospheric and modeling community is to push the starting time of the model runs further back into time. The MEPED/POES SEM-2 we use in the current study start with the beginning of NOAA-15 operations on 1 July 1998, while MEPED/POES SEM-1 observations began with NOAA-5 in November 1978 and end with NOAA-14 in December 2004. However, climate models are regularly run with significantly earlier start dates, suggesting that more focus on proxies for EEP, for example, using simple geomagnetic indices, might be required. Finally, if EEP is to be regularly incorporated into climate model runs, consideration should be given to the ease of use for the climate modelers. This appears to be one of the strengths of the AIMOS model.

8. Summary and Conclusions

One of the most commonly used sources of EEP measurements are MEPED/POES spacecraft observations. As these spacecraft observations have been made with essentially the same instruments for more than 15 years, they have naturally been the focus of researchers wishing to incorporate EEP into various models. They have also been subject to increasing scrutiny due to the growing evidence that EEP leads to significant mesospheric changes in the polar atmosphere which may influence midlatitude and high-latitude surface climates. However, there are numerous concerns and issues surrounding the MEPED/POES EEP measurements, causing uncertainty as to the suitability of their use in such models. We have therefore attempted to make an independent set of long EEP observations by exploiting a ground-based data to compare and contrast with those provided by MEPED/POES.

We have analyzed observations of subionospherically propagating VLF radio waves to determine the outer radiation belt EEP flux magnitudes. The AARDDVARK radio wave receivers in Sodankylä, Finland (SGO), have monitored the U.S. Navy transmitter with call sign NAA (Cutler, Maine) near continuously across the time period spanning November 2004 until December 2013. Building on an earlier study by *Clilverd et al*. [2010], we have improved upon the data set, data analysis, and modeling to determine the long time period EEP variations.

Our experimental observations include 2859 days worth of good quality NAA-SGO amplitude measurements at 1 min resolution. At this point, we are limited to EEP extraction for the summer period; the NAA-SGO observations were used to generate 693 days worth of EEP flux magnitude values at 1 h resolutions. These AARDDVARK-based fluxes agree rather well with the essentially independent MEPED/POES precipitation measurements during high-intensity precipitation events. Our AARDDVARK observations provide additional confidence that the MEPED/POES precipitation fluxes are reasonable during geomagnetic storms, confirming other recent studies. However, the AARDDVARK EEP observations fall to much lower flux magnitudes than MEPED/POES, indicating that our method of EEP detection is 10–50 times more sensitive to low flux levels than the satellite measurements, largely due to the high-noise floor of the MEPED/POES telescopes. Our EEP

variations show a good agreement with the variation in lower band chorus wave powers, providing some confidence that chorus is the primary driver for the outer belt precipitation we are monitoring.

This work continues our efforts to validate EEP fluxes and to exploit the long AARDDVARK subionospheric observation data set. At this point, our EEP extraction approaches are limited to summer periods on the NAA-SGO path. We are investigating different analyses and modeling approaches which would allow us to extend to a wide range of ionospheric conditions. This is likely to lead to at least a doubling of the EEP data set we have generated in the current study.

Finally, we presented the result of some initial data quality checks into the outputs of the version 1.2 Atmospheric Ionization Module OSnabrück (AIMOS) model which purports to provide 3-D time-varying numerical information on atmospheric ionization due to precipitating particles. We showed evidence that there are numerous serious data quality problems in the AIMOS model outputs, some due to contamination issues in the input data and others inherent to the model. AIMOS v1.2 ionization rates are unlikely to be accurate in the mesosphere and upper stratosphere during geomagnetically quiet times, for middle and low latitudes, during solar proton events, or during geomagnetic storms. The validity of modeling studies making use of AIMOS v1.2 is questionable, and great care must be taken when considering the conclusions of such studies.

Acknowledgments

The authors would like to thank the researchers and engineers of NOAA's Space Environment Center for the provision of the data and the operation of the SEM-2 instrument carried on board these spacecraft. J.J.N. was supported by the University of Otago via a Research Master's Scholarship and a Postgraduate Publishing Bursary. C.J.R. and J.J.N. were (partly) supported by the New Zealand Marsden Fund. M.A.C. was supported by the Natural Environmental Research Council grant NE/J008125/1. Data availability is described at the following websites: http://www.physics.otago.ac.nz/space/AARDDVARK_homepage.htm (AARDDVARK), http://satdat.ngdc.noaa.gov/sem/poes/data/ (POES SEM-2), and http://aimos.physik.uos.de/ (AIMOS).

Michael Liemohn thanks Adam Kellerman and another reviewer for their assistance in evaluating this paper.

References

Andersson, M. E., P. T. Verronen, S. Wang, C. J. Rodger, M. A. Clilverd, and B. R. Carson (2012), Precipitating radiation belt electrons and enhancements of mesospheric hydroxyl during 2004–2009, *J. Geophys. Res.*, *117*, D09304, doi:10.1029/2011JD017246.

Andersson, M. E., P. T. Verronen, C. J. Rodger, M. A. Clilverd, and S. Wang (2014a), Longitudinal hot spots in the mesospheric OH variations due to energetic electron precipitation, *Atmos. Chem. Phys.*, *14*, 1095–1105, doi:10.5194/acp-14-1095-2014.

Andersson, M., P. T. Verronen, C. J. Rodger, M. A. Clilverd, and A. Seppälä (2014b), Missing driver in the Sun-Earth connection from energetic electron precipitation impacts mesospheric ozone, *Nat. Commun.*, *5*, 5197, doi:10.1038/ncomms6197.

Baumgaertner, A. J. G., A. Seppälä, P. Joeckel, and M. A. Clilverd (2011), Geomagnetic activity related NO_x enhancements and polar surface air temperature variability in a chemistry-climate model: Modulation of the NAM index, *Atmos. Chem. Phys.*, *11*(9), 4521–4531, doi:10.5194/acp-11-4521-2011.

Berthelier, J. J., et al. (2006), ICE: The electric field experiment on DEMETER, *Planet. Space Sci.*, *54*(5), 456–471.

Brasseur, G., and S. Solomon (2005), *Aeronomy of the Middle Atmosphere: Chemistry and Physics of the Stratosphere and Mesosphere*, 3rd ed., D. Reidel, Dordrecht, Netherlands.

Clilverd, M. A., et al. (2009), Remote sensing space weather events: The AARDDVARK network, *Space Weather*, *7*, S04001, doi:10.1029/2008SW000412.

Clilverd, M. A., C. J. Rodger, R. J. Gamble, T. Ulich, T. Raita, A. Seppälä, J. C. Green, N. R. Thomson, J.-A. Sauvaud, and M. Parrot (2010), Ground-based estimates of outer radiation belt energetic electron precipitation fluxes into the atmosphere, *J. Geophys. Res.*, *115*, A12304, doi:10.1029/2010JA015638.

Clilverd, M. A., C. J. Rodger, D. Danskin, M. E. Usanova, T. Raita, T. Ulich, and E. L. Spanswick (2012), Energetic particle injection, acceleration, and loss during the geomagnetic disturbances which upset Galaxy 15, *J. Geophys. Res.*, *117*, A12213, doi:10.1029/2012JA018175.

Clilverd, M. A., C. J. Rodger, M. Andersson, P. T. Verronen, and A. Seppälä (2015), Linkages between the radiation belts, polar atmosphere and climate: Electron precipitation through wave particle interactions, in *Waves, Particles and Storms in Geospace*, edited by I. Mann et al., Oxford Univ. Press, in press.

Cresswell-Moorcock, K., C. J. Rodger, A. Kero, A. B. Collier, M. A. Clilverd, I. Häggström, and T. Pitkänen (2013), A reexamination of latitudinal limits of substorm-produced energetic electron precipitation, *J. Geophys. Res. Space Physics*, *118*, 6694–6705, doi:10.1002/jgra.50598.

Daae, M., P. Espy, H. Nesse Tyssøy, D. Newnham, J. Stadsnes, and F. Søraas (2012), The effect of energetic electron precipitation on middle mesospheric nighttime ozone during and after a moderate geomagnetic storm, *Geophys. Res. Lett.*, *39*, L21811, doi:10.1029/2012GL053787.

Dowden, R. L., S. F. Hardman, C. J. Rodger, and J. B. Brundell (1998), Logarithmic decay and Doppler shift of plasma associated with sprites, *J. Atmos. Sol. Terr. Phys.*, *60*, 741–753, doi:10.1016/S1364-6826(98)00019-4.

Evans, D. S., and M. S. Greer (2004), Polar-orbiting Environmental Satellite Space Environment Monitor-2 instrument descriptions and archive data documentation, NOAA Tech. Memorandum version 1.4, Space Environment Laboratory, Colo.

Ferguson, J. A., and F. P. Snyder (1990), Computer programs for assessment of long wavelength radio communications, Tech. Doc. 1773, Natl. Ocean Syst. Cent., San Diego, Calif.

Friedrich, M., D. E. Siskind, and K. M. Torkar (1998), Haloe nitric oxide measurements in view of ionospheric data, *J. Atmos. Sol. Terr. Phys.*, *60*(15), 1445–1457, doi:10.1016/S1364-6826(98)00091-1.

Funke, B., et al. (2011), Composition changes after the "Halloween" solar proton event: The High Energy Particle Precipitation in the Atmosphere (HEPPA) model versus MIPAS data intercomparison study, *Atmos. Chem. Phys.*, *11*, 9089–9139, doi:10.5194/acp-11-9089-2011.

Goldberg, R. A., C. H. Jackman, J. R. Barcus, and F. Søraas (1984), Nighttime auroral energy deposition in the middle atmosphere, *J. Geophys. Res.*, *89*(A7), 5581–5596, doi:10.1029/JA089iA07p05581.

Hargreaves, J. K., M. J. Birch, and D. S. Evans (2010), On the fine structure of medium energy electron fluxes in the auroral zone and related effects in the ionospheric *D* region, *Ann. Geophys.*, *28*, 1107–1120, doi:10.5194/angeo-28-1107-2010.

Hendry, A. T., C. J. Rodger, M. A. Clilverd, N. R. Thomson, S. K. Morley, and T. Raita (2012), Rapid radiation belt losses occurring during high-speed solar wind stream-driven storms: Importance of energetic electron precipitation, in *Dynamics of the Earth's Radiation Belts and Inner Magnetosphere*, edited by D. Summers et al., pp. 213–224, AGU, Washington, D. C., doi:10.1029/2012GM001299.

Horne, R. B., S. A. Glauert, and R. M. Thorne (2003), Resonant diffusion of radiation belt electrons by whistler mode chorus, *Geophys. Res. Lett.*, *30*(9), 1493, doi:10.1029/2003GL016963.

Jackman, C. H., D. R. Marsh, F. M. Vitt, R. R. Garcia, C. E. Randall, E. L. Fleming, and S. M. Frith (2009), Long-term middle atmospheric influence of very large solar proton events, *J. Geophys. Res.*, *114*, D11304, doi:10.1029/2008JD011415.

Lam, M. M., R. B. Horne, N. P. Meredith, S. A. Glauert, T. Moffat-Griffin, and J. C. Green (2010), Origin of energetic electron precipitation >30 keV into the atmosphere, *J. Geophys. Res.*, *115*, A00F08, doi:10.1029/2009JA014619.

Li, X., and M. Temerin (2001), The electron radiation belt, *Space Sci. Rev.*, *95*(1–2), 569–580, doi:10.1023/A:1005221108016.

Li, W., B. Ni, R. M. Thorne, J. Bortnik, J. C. Green, C. A. Kletzing, W. S. Kurth, and G. B. Hospodarsky (2013), Constructing the global distribution of chorus wave intensity using measurements of electrons by the POES satellites and waves by the Van Allen Probes, *Geophys. Res. Lett.*, *40*, 4526–4532, doi:10.1002/grl.50920.

Lorentzen, K. R., J. B. Blake, U. S. Inan, and J. Bortnik (2001), Observations of relativistic electron microbursts in association with VLF chorus, *J. Geophys. Res.*, *106*(A4), 6017–6027, doi:10.1029/2000JA003018.

McRae, W. M., and N. R. Thomson (2000), VLF phase and amplitude: Daytime ionospheric parameters, *J. Atmos. Sol. Terr. Phys.*, *62*(7), 609–618.

Meredith, N. P., R. B. Horne, M. M. Lam, M. H. Denton, J. E. Borovsky, and J. C. Green (2011), Energetic electron precipitation during high-speed solar wind stream driven storms, *J. Geophys. Res.*, *116*, A05223, doi:10.1029/2010JA016293.

Millan, R. M., and R. M. Thorne (2007), Review of radiation belt relativistic electron loss, *J. Atmos. Sol. Terr. Phys.*, *69*, 362–377, doi:10.1016/j.jastp.2006.06.019.

Morley, S. K., R. H. W. Friedel, E. L. Spanswick, G. D. Reeves, J. T. Steinberg, J. Koller, T. Cayton, and E. Noveroske (2010), Dropouts of the outer electron radiation belt in response to solar wind stream interfaces: Global positioning system observations, *Proc. R. Soc. A*, *466*(2123), 3329–3350, doi:10.1098/rspa.2010.0078.

Newnham, D. A., P. J. Espy, M. A. Clilverd, C. J. Rodger, A. Seppälä, D. J. Maxfield, P. Hartogh, K. Holmén, and R. B. Horne (2011), Direct observations of nitric oxide produced by energetic electron precipitation in the Antarctic middle atmosphere, *Geophys. Res. Lett.*, *38*, L20104, doi:10.1029/2011GL049199.

Ni, B., J. Bortnik, R. M. Thorne, Q. Ma, and L. Chen (2013), Resonant scattering and resultant pitch angle evolution of relativistic electrons by plasmaspheric hiss, *J. Geophys. Res. Space Physics*, *118*, 7740–7751, doi:10.1002/2013JA019260.

Ni, B., W. Li, R. M. Thorne, J. Bortnik, J. C. Green, C. A. Kletzing, W. S. Kurth, G. B. Hospodarsky, and M. de Soria-Santacruz Pich (2014), A novel technique to construct the global distribution of whistler mode chorus wave intensity using low-altitude POES electron data, *J. Geophys. Res. Space Physics*, *119*, 5685–5699, doi:10.1002/2014JA019935.

Picone, J. M., A. E. Hedin, D. P. Drob, and A. C. Aikin (2002), NRLMSISE-00 empirical model of the atmosphere: Statistical comparisons and scientific issues, *J. Geophys. Res.*, *107*(A12), 1468, doi:10.1029/2002JA009430.

Pincon, J.-L., E. Blanc, P.-L. Blelly, M. Parrot, J.-L. Rauch, J.-A. Savaud, and E. Seran (2011), TARANIS: Scientific payload and mission strategy, in *General Assembly and Scientific Symposium 2011 XXXth URSI*, pp. 1–4, IEEE, Istanbul, doi:10.1109/URSIGASS.2011.6050938.

Rees, M. H. (1989), *Physics and Chemistry of the Upper Atmosphere*, Cambridge Univ. Press, Cambridge, U. K.

Reeves, G. D., K. L. McAdams, R. H. W. Friedel, and T. P. O'Brien (2003), Acceleration and loss of relativistic electrons during geomagnetic storms, *Geophys. Res. Lett.*, *30*(10), 1529, doi:10.1029/2002GL016513.

Reeves, G., A. Chan, and C. J. Rodger (2009), New directions for radiation belt research, *Space Weather*, *7*, S07004, doi:10.1029/2008SW000436.

Rodger, C. J., O. A. Molchanov, and N. R. Thomson (1998), Relaxation of transient ionization in the lower ionosphere, *J. Geophys. Res.*, *103*(A4), 6969–6975, doi:10.1029/98JA00016.

Rodger, C. J., M. A. Clilverd, P. T. Verronen, T. Ulich, M. J. Jarvis, and E. Turunen (2006), Dynamic geomagnetic rigidity cutoff variations during a solar proton event, *J. Geophys. Res.*, *111*, A04222, doi:10.1029/2005JA011395.

Rodger, C. J., M. A. Clilverd, N. R. Thomson, R. J. Gamble, A. Seppälä, E. Turunen, N. P. Meredith, M. Parrot, J.-A. Sauvaud, and J.-J. Berthelier (2007a), Radiation belt electron precipitation into the atmosphere: Recovery from a geomagnetic storm, *J. Geophys. Res.*, *112*, A11307, doi:10.1029/2007JA012383.

Rodger, C. J., C. F. Enell, E. Turunen, M. A. Clilverd, N. R. Thomson, and P. T. Verronen (2007b), Lightning-driven inner radiation belt energy deposition into the atmosphere: Implications for ionization levels and neutral chemistry, *Ann. Geophys.*, *25*, 1745–1757.

Rodger, C. J., M. A. Clilverd, J. C. Green, and M. M. Lam (2010a), Use of POES SEM-2 observations to examine radiation belt dynamics and energetic electron precipitation into the atmosphere, *J. Geophys. Res.*, *115*, A04202, doi:10.1029/2008JA014023.

Rodger, C. J., M. A. Clilverd, A. Seppälä, N. R. Thomson, R. J. Gamble, M. Parrot, J. A. Sauvaud, and T. Ulich (2010b), Radiation belt electron precipitation due to geomagnetic storms: Significance to middle atmosphere ozone chemistry, *J. Geophys. Res.*, *115*, A11320, doi:10.1029/2010JA015599.

Rodger, C. J., M. A. Clilverd, A. J. Kavanagh, C. E. J. Watt, P. T. Verronen, and T. Raita (2012), Contrasting the responses of three different ground-based instruments to energetic electron precipitation, *Radio Sci.*, *47*, RS2021, doi:10.1029/2011RS004971.

Rodger, C. J., A. J. Kavanagh, M. A. Clilverd, and S. R. Marple (2013), Comparison between POES energetic electron precipitation observations and riometer absorptions: Implications for determining true precipitation fluxes, *J. Geophys. Res. Space Physics*, *118*, 7810–7821, doi:10.1002/2013JA019439.

Rodger, C. J., M. A. Clilverd, J. M. Wissing, A. J. Kavanagh, T. Raita, and S. Marple (2014), Testing AIMOS ionization rates in the middle atmosphere: Comparison with ground-based radio wave observations of the ionosphere, 31st General Assembly of the International Union of Radio Science, Beijing, China.

Rozanov, E., L. Callis, M. Schlesinger, F. Yang, N. Andronova, and V. Zubov (2005), Atmospheric response to NO_y source due to energetic electron precipitation, *Geophys. Res. Lett.*, *32*, L14811, doi:10.1029/2005GL023041.

Russell, C. T., J. G. Luhmann, and L. K. Jian (2010), How unprecedented a solar minimum is?, *Rev. Geophys.*, *48*, RG2004, doi:10.1029/2009RG000316.

Saito, S., Y. Miyoshi, and K. Seki (2012), Relativistic electron microbursts associated with whistler chorus rising tone elements: GEMSIS-RBW simulations, *J. Geophys. Res.*, *117*, A10206, doi:10.1029/2012JA018020.

Santolík, O., J. Chum, M. Parrot, D. A. Gurnett, J. S. Pickett, and N. Cornilleau-Wehrlin (2006), Propagation of whistler mode chorus to low altitudes: Spacecraft observations of structured ELF hiss, *J. Geophys. Res.*, *111*, A10208, doi:10.1029/2005JA011462.

Seppälä, A., P. T. Verronen, V. F. Sofieva, J. Tamminen, E. Kyrölä, C. J. Rodger, and M. A. Clilverd (2006), Destruction of the tertiary ozone maximum during a solar proton event, *Geophys. Res. Lett.*, *33*, L07804, doi:10.1029/2005GL025571.

Seppälä, A., M. A. Clilverd, and C. J. Rodger (2007), NO_x enhancements in the middle atmosphere during 2003–2004 polar winter: Relative significance of solar proton events and the aurora as a source, *J. Geophys. Res.*, *112*, D23303, doi:10.1029/2006JD008326.

Seppälä, A., C. E. Randall, M. A. Clilverd, E. Rozanov, and C. J. Rodger (2009), Geomagnetic activity and polar surface level air temperature variability, *J. Geophys. Res.*, *114*, A10312, doi:10.1029/2008JA014029.

Seppälä, A., H. Lu, M. A. Clilverd, and C. J. Rodger (2013), Geomagnetic activity signatures in wintertime stratosphere-troposphere temperature, wind, and wave response, *J. Geophys. Res. Atmos.*, *118*, 2169–2183, doi:10.1002/jgrd.50236.

Simon Wedlund, M., M. A. Clilverd, C. J. Rodger, K. Cresswell-Moorcock, N. Cobbett, P. Breen, D. Danskin, E. Spanswick, and J. V. Rodriguez (2014), A statistical approach to determining energetic outer radiation belt electron precipitation fluxes, *J. Geophys. Res. Space Physics*, *119*, 3961–3978, doi:10.1002/2013JA019715.

Tan, L. C., S. F. Fung, and X. Shao (2007), NOAA/POES MEPED data documentation: NOAA-5 to NOAA-14 data reprocessed at GSFC/SPDF, NASA Space Physics Data Facility.

Thomson, N. R., and M. A. Clilverd (2000), Solar cycle changes in daytime VLF subionospheric attenuation, *J. Atmos. Sol. Terr. Phys.*, *62*(7), 601–608, doi:10.1016/S1364-6826(00)00026-2.

Thorne, R. M. (1977), Energetic radiation belt electron precipitation: A natural depletion mechanism for stratospheric ozone, *Science*, *195*, 287–289.

Thorne, R. M. (2010), Radiation belt dynamics: The importance of wave-particle interactions, *Geophys. Res. Lett.*, *37*, L22107, doi:10.1029/2010GL044990.

Thorne, R. M., T. P. O'Brien, Y. Y. Shprits, D. Summers, and R. B. Horne (2005), Timescale for MeV electron microburst loss during geomagnetic storms, *J. Geophys. Res.*, *110*, A09202, doi:10.1029/2004JA010882.

Tu, W., R. Selesnick, X. Li, and M. Looper (2010), Quantification of the precipitation loss of radiation belt electrons observed by SAMPEX, *J. Geophys. Res.*, *115*, A07210, doi:10.1029/2009JA014949.

Turner, D. L., Morley, S. K., Miyoshi, Y., Ni, B., and Huang, C.-L. (2012), Outer radiation belt flux dropouts: Current understanding and unresolved questions, in *Dynamics of the Earth's Radiation Belts and Inner Magnetosphere*, edited by D. Summers et al., pp. 195–212, AGU, Washington, D. C., doi:10.1029/2012GM001310.

Turunen, E., P. T. Verronen, A. Seppälä, C. J. Rodger, M. A. Clilverd, J. Tamminen, C. F. Enell, and T. Ulich (2009), Impact of different energies of precipitating particles on NO_x generation in the middle and upper atmosphere during geomagnetic storms, *J. Atmos. Sol. Terr. Phys.*, *71*, 1176–1189, doi:10.1016/j.jastp.2008.07.005.

Verronen, P. T., C. J. Rodger, M. A. Clilverd, and S. Wang (2011), First evidence of mesospheric hydroxyl response to electron precipitation from the radiation belts, *J. Geophys. Res.*, *116*, D07307, doi:10.1029/2010JD014965.

Wait, J. R., and K. P. Spies (1964), Characteristics of the Earth-ionosphere waveguide for VLF radio waves, NBS Tech. Note 300, Nat. Inst. of Stand. and Technol., Gaithersburg, Md.

Whittaker, I. C., R. J. Gamble, C. J. Rodger, M. A. Clilverd, and J.-A. Sauvaud (2013), Determining the spectra of radiation belt electron losses: Fitting DEMETER electron flux observations for typical and storm times, *J. Geophys. Res. Space Physics*, *118*, 7611–7623, doi:10.1002/2013JA019228.

Whittaker, I. C., C. J. Rodger, M. A. Clilverd, and J.-A. Sauvaud (2014), The effects and correction of the geometric factor for the POES/MEPED electron flux instrument using a multisatellite comparison, *J. Geophys. Res. Space Physics*, *119*, 6386–6404, doi:10.1002/2014JA020021.

Wissing, J. M., and M.-B. Kallenrode (2009), Atmospheric Ionization Module OSnabrück (AIMOS): A 3-D model to determine atmospheric ionization by energetic charged particles from different populations, *J. Geophys. Res.*, *114*, A06104, doi:10.1029/2008JA013884.

Wissing, J. M., M.-B. Kallenrode, J. Kieser, H. Schmidt, M. T. Rietveld, A. Strømme, and P. J. Erickson (2011), Atmospheric Ionization Module OSnabrück (AIMOS): 3. Comparison of electron density simulations by AIMOS-HAMMONIA and incoherent scatter radar measurements, *J. Geophys. Res.*, *116*, A08305, doi:10.1029/2010JA016300.

Yando, K., R. M. Millan, J. C. Green, and D. S. Evans (2011), A Monte Carlo simulation of the NOAA POES Medium Energy Proton and Electron Detector instrument, *J. Geophys. Res.*, *116*, A10231, doi:10.1029/2011JA016671.

Zhima, Z., J. Cao, W. Liu, H. Fu, J. Yang, X. Zhang, and X. Shen (2013), DEMETER observations of high-latitude chorus waves penetrating the plasmasphere during a geomagnetic storm, *Geophys. Res. Lett.*, *40*, 5827–5832, doi:10.1002/2013GL058089.